Astronomy & Astrophysics manuscript no. B59
May 6, 2022

The molecular gas content of the Pipe Nebula

I. Direct evidence of outflow-generated turbulence in B59?

A. Duarte-Cabral[1,2,3], A. Chrysostomou[4], N. Peretto[5], G. A. Fuller[3], B. Matthews[6,7], G. Schieven[6,7], and G. R. Davis[4]

[1] Univ. Bordeaux, LAB, UMR 5804, F-33270, Floirac, France.
[2] CNRS, LAB, UMR 5804, F-33270, Floirac, France
[3] Jodrell Bank Centre for Astrophysics, School of Physics and Astronomy, University of Manchester, Oxford Road, Manchester, M13 9PL, U.K.
[4] Joint Astronomy Centre, 660 North Aohoku Place, Hilo, HI 96720, USA
[5] Laboratoire AIM, CEA/DSM-CNRS-Université Paris Diderot, IRFU/Service d'Astrophysique, C.E. Saclay, Orme de merisiers, 91191 Gif-sur-Yvette, France
[6] Herzberg Institute of Astrophysics, National Research Council Canada, 5071 West Saanich Road., Victoria, BC, Canada, V9E 2E7, Canada
[7] University of Victoria, Finnerty Road, Victoria, BC, V8W 3P6 Canada

Received 18 March 2012; accepted 12 May 2012

ABSTRACT

Context. Star forming regions may share many characteristics, but the specific interplay between gravity, magnetic fields, large-scale dynamics, and protostellar feedback will have an impact on the specific star formation history of each region. The particular importance of outflows is subject of debate, where we are yet to understand whether they can input and sustain turbulence in the cloud, and if this turbulence is enough to support the cloud and prevent further fragmentation.
Aims. The Pipe Nebula is a molecular cloud hosting the B59 region as its only active star-forming clump. The quiet nature of the gas in this cloud makes B59 a good site to directly see the impact of protostellar feedback on the quiescent dense gas. This paper focuses on a study of the global dynamics of B59, its temperature structure, and its outflowing gas, with the goal of revealing the local and global impact of the protostellar outflows.
Methods. Using HARP at the JCMT, we mapped the B59 region with the $J = 3 \rightarrow 2$ transition of ^{12}CO to study the kinematics and energetics of the outflows, and ^{13}CO and C^{18}O to study the overall dynamics of the ambient cloud, the physical properties of the gas, and the hierarchical structure of the region.
Results. The B59 region has a total of ~ 30 M$_\odot$ of cold and quiescent material, mostly gravitationally bound, with narrow line widths throughout. Such low levels of turbulence in non-star-forming sites of B59 are indicative of the intrinsic initial conditions of the cloud. On the other hand, close to the forming protostars the impact of the outflows is observed as a localised increase of both line widths from ~ 0.3 km s^{-1} to ~ 1 km s^{-1}, and ^{13}CO excitation temperatures by $\sim 2-3$K. The impact of the outflows is also evident in the low column density material which shows signs of being pushed, shaped and carved by the outflow bow shocks as they pierce their way out of the cloud. Much of this structure is readily apparent in a dendrogram analysis of the cloud.
Conclusions. B59's low mass, intrinsically quiescent gas and small number of protostars, allows the identification of specific regions of the outflows' interaction with the dense gas. Our study suggests that outflows are an important mechanism in injecting and sustaining supersonic turbulence at sub-parsec scales. We find that only a fraction, i.e. less than half, of the outflow energy is deposited as turbulent energy of the gas. This turbulent energy is sufficient to slow down the collapse of the region.

Key words. Stars: formation, protostars; ISM: clouds, jets and outflows, kinematics and dynamics, individual objects: B59

1. Introduction

As stellar nurseries, molecular clouds contain the ingredients for star formation. However, the physical processes which prevent or trigger star formation are subjects of debate over the past years (e.g. McKee & Ostriker 2007; Vazquez-Semadeni 2010; Hennebelle & Chabrier 2011). The relative importance of each physical ingredient is most likely not universal, and while some regions experience dynamical conditions such as a collision of clouds or convergence of flows (e.g. Vázquez-Semadeni et al. 2007; Schneider et al. 2010; Duarte-Cabral et al. 2011), others can evolve more quietly, from quiescent material possibly supported and governed by the local magnetic field (e.g. Nakamura & Li 2008; Alves et al. 2008). The imprints of the initial conditions specific to a given cloud are often still seen in the properties of the gas and dust of young proto-clusters. However, as soon as star formation begins to take place, what we observe is the superimposed effect of these initial conditions and the feedback from the forming stars.

Young protostellar outflows may be responsible for clearing up and disrupting the protostellar envelopes, limiting the reservoir of mass which will end up being accreted (e.g. Fuller & Ladd 2002; Arce & Sargent 2006; Arce et al. 2010). Even though outflows may carry sufficient energy to unbind the material, this energy may well be deposited far from the dense gas, or even outside the molecular cloud. Knowing exactly where this momentum and energy is deposited is fundamental to understand if outflows are a source of turbulence capable of providing a sup-

Send offprint requests to: Ana Duarte Cabral, e-mail: Ana.Cabral@obs.u-bordeaux1.fr

port against gravity and slow down star formation. However, the efficiency of such outflow-generated turbulence is strongly debated (see review from McKee & Ostriker 2007). The analytical model from Matzner & McKee (2000) estimates a typical outflow injection scale, i.e. the scale at which the momentum is more efficiently deposited, of a few tenths of parsec. MHD numerical models (e.g. Nakamura & Li 2007; Carroll et al. 2009, 2010) have also shown that, even though outflows are not the primary source of turbulence at all scales in molecular clouds, they can drive supersonic turbulence at sub-outflow scales and produce smooth velocity structures on outflow-scales that sweep up and dissipate smaller structures. This produces an overall flatter density spectrum, which limits the fragmentation and infall material onto the final protostars.

Observationally, it is suggested that outflows hardly provide enough kinetic energy to support the entire cloud against gravity (e.g. Arce et al. 2010; Maury et al. 2009), even though they may be able to maintain the supersonic turbulence at sub-parsec scales (e.g. Nakamura et al. 2011). Nevertheless, the outflow importance on the energy balance of a region is likely to depend on the physical properties of the system and initial conditions of the star-forming region. Furthermore, observational studies have difficulties in determining if outflows can halt star formation, and in measuring the direct injection of turbulence due to the outflows. One reason why such study is complicated arises from the fact that in dynamic cluster-forming regions, with large-scale motions, and on-going star formation, the direct effect of outflows can be easily confused and masked out by other dynamical events.

Here we present a study of the B59 star-forming region, within the generally quiescent Pipe Nebula. In a low-density quiescent cloud such as the Pipe, we have the opportunity to see the direct impact of outflows where stars have began to form. In Sect. 2 we present an overview of the Pipe Nebula and its active portion, B59. In Sect. 3 we detail the observations. We present the results on the physical properties in Sect. 4, including optical depth and estimates of excitation temperatures. The outflows of the region are presented in Sect. 5. The ambient cloud's dynamics and hierarchical structure are described in Sect. 6 (the details on the hierarchical structure of B59, performed using a dendrogram technique, is described in detail in Appendix A). Finally, we discuss the outflow-dense gas interaction in Sect. 7, and we outline our conclusions in Sect. 8.

2. The Pipe Nebula and B59

The Pipe Nebula, located at ~ 130 pc[1] from the Sun (Lombardi et al. 2006), is one of the Gould Belt of star-forming regions. Although the global features of this cloud appear similar to other Gould Belt clouds, with a total mass comparable to the few $\times 10^4$ $M_\odot$ of the Taurus-Auriga complex, and a filamentary structure with a magnetic field threading through it (Alves et al. 2008), it has an extremely low star formation efficiency (less than 0.1%) compared to other Gould Belt clouds (2-20%). In fact, only one active star forming clump, B59, has been found so far in the whole cloud (Brooke et al. 2007; Forbrich et al. 2009, 2010). This small group of protostars within B59 are known to power more than one molecular outflow (Onishi et al. 1999; Riaz et al. 2009). Figure 1 shows the extinction map of B59 and identifies several features and regions which will be referred to in the analysis discussed in this work.

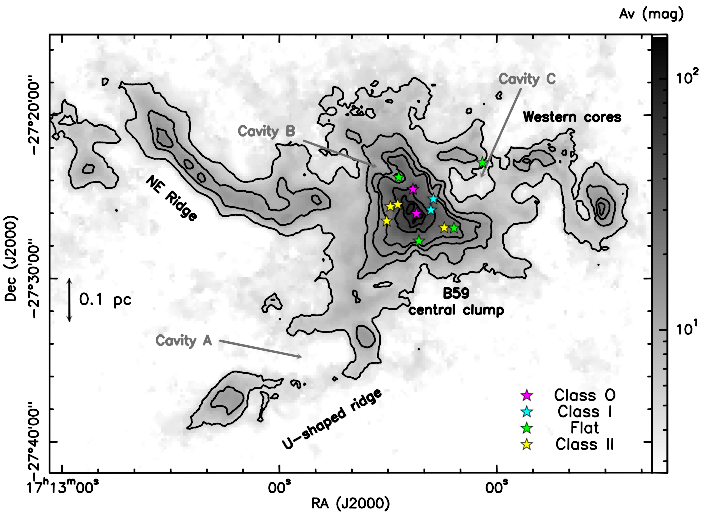

Fig. 1. Extinction map of B59 in gray scale and contours (Román-Zúñiga et al. 2009), showing the known YSOs in the region (from Brooke et al. 2007; Forbrich et al. 2009), except for the Class III objects. Contours are from an A_v of 5 to 20 by steps of 5, and then by steps of 20. Note that there are only four known protostars (between Class 0 and I). The black labels show the designation of regions within B59 as adopted throughout the paper. Some cavities are also pointed out with grey arrows and labels, and discussed further in the text.

Several scenarios have been suggested for the formation of B59 as an active star-forming clump at the edge of the Pipe Nebula. One scenario suggests that B59 is formed due to a gravitational focus point on an evolution solely governed by gravity (Heitsch et al. 2009). In another view, the non-negligible strength and morphology of the magnetic field, in tight connection to the shape of the Pipe Nebula, are suggested to be playing an important role as guide-lines for the collapse of material towards the main filament (Alves et al. 2008). Peretto et al. (2012) propose that the formation of B59 at the edge of the Pipe is due to a compression front (at the west end of the B59, beyond the western cores) from a nearby OB association which allowed to gather mass in a "snow-plough" fashion. The effects of gravitational focusing would play a role later on, with a contraction of the gathered gas and allowing the formation of stars in the centre of B59.

Our knowledge of the molecular gas structure in the Pipe Nebula, however, was limited to the 4′ resolution maps of the $J = 1 \rightarrow 0$ transitions of ^{12}CO, ^{13}CO and C^{18}O by Onishi et al. (1999). Beyond this, molecular line observations of the Pipe Nebula consist of single spectra of dense gas tracers such as NH_3, CCS, HC_5N and other early- and late-time molecules (Rathborne et al. 2008; Frau et al. 2010, 2012), and C^{18}O (Muench et al. 2007) towards the peaks of cores identified in the 1′ resolution extinction maps (Lombardi et al. 2006; Román-Zúñiga et al. 2010).

3. Observations

Using HARP at the JCMT (Buckle et al. 2009) in May and June 2010, we have mapped ^{13}CO and C^{18}O $J = 3 \rightarrow 2$ (at 330.6

[1] Alves & Franco (2007) have estimated a distance of 145 pc, but we are adopting 130 pc as it lies within the uncertainties of these authors, and it has been the distance most commonly adopted in other studies of the Pipe Nebula. We note, however, that the uncertainties on the distance are of the order of 10% and we are therefore possibly underestimating masses by 20% by assuming the nearer 130 pc distance.

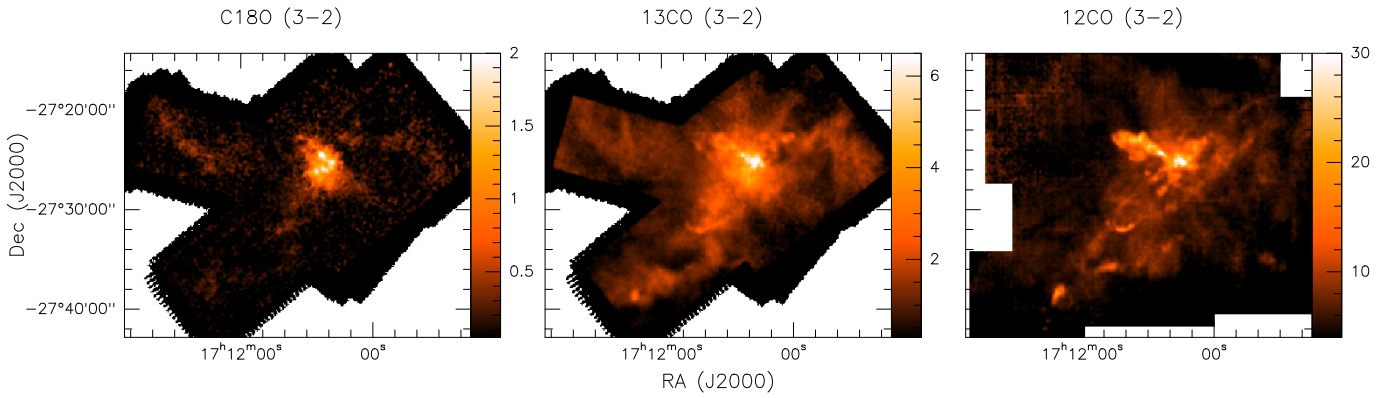

Fig. 2. Integrated intensity maps of the three isotopologues observed, in units of T_A^* (K). For the $C^{18}O$ (left) and ^{13}CO (middle), the integration was made from 1 to 5.5 km s^{-1}. The ^{12}CO (right) was integrated from -5 to 15 km s^{-1}. Here we can see that the $C^{18}O$ follows the shape as seen in extinction (Fig. 1), while the ^{13}CO emission starts to pick up the outflowing material, best seen in the ^{12}CO emission dominated by high velocity gas.

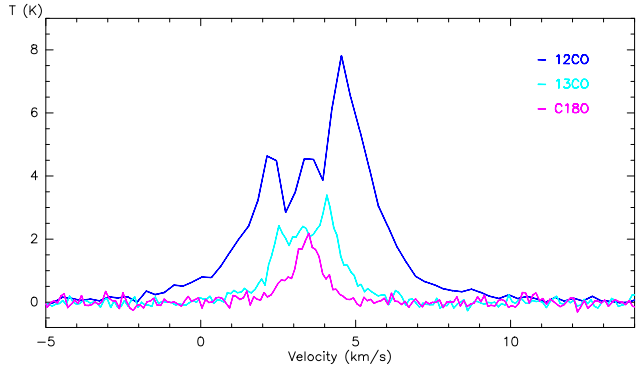

Fig. 3. Overplot of a spectrum of $C^{18}O$ (purple line), ^{13}CO (light blue line), with a velocity resolution of 0.1 kms^{-1}, and ^{12}CO (dark blue line), with a velocity resolution of 0.3 kms^{-1}, in B59, at the position of the Class 0 source B11, at RA = 17^{h}11^{m}23.0^s and Dec = -27°24'32.8", showing the outflow wings and self absorption dip in ^{13}CO and ^{12}CO.

and 329.3 GHz respectively) in the entire B59 star-forming region (~ 0.11 deg^2). All observations were taken with a sky opacity at 225GHz varying between 0.05 and 0.08. These data were taken as several raster maps which have an original spatial resolution of 15″ and a spectral resolution of 0.05 kms^{-1}. The r.m.s. noise level on the final B59 dataset is 0.22 K (in T_A^*) with 0.25 kms^{-1} channels. A complementary ^{12}CO $J = 3 \rightarrow 2$ (at 345.8 GHz) deep and high resolution (15") map of B59 has been carried out with HARP using JCMT Director's discretion telescope time. These data reached a 0.2 K noise level (in T_A^*) at 0.5 kms^{-1} velocity resolution. The telescope main beam efficiency is $\eta_{mb} = 0.66$ (Buckle et al. 2009; Curtis et al. 2010a) for the three observed molecular transitions.

The data reduction was performed using the ORAC-DR pipeline, using the recipe REDUCE SCIENCE NARROWLINE, without applying the recipe's flatfield algorithm (designed to suppress stripping in the map due to bad receptors), and with a pixel size of 7.4″. This reduction procedure automatically fits and corrects the baselines and removes the bad detectors based on the time-series data and on the r.m.s. noise levels of the final maps. The final reduced maps of each area were gridded together using the Starlink software (integrated intensity maps in Fig. 2, example of spectra on Fig. 3).

The science handling of the data was made after convolving all datacubes to a 20″ resolution, in order to suppress some of the high frequency noise, and after masking the datacubes to pixels where the peak signal to noise (estimated at each pixel) was higher than 4 in the smoothed map. This masking procedure was particularly effective for the weaker $C^{18}O$, but it left virtually unchanged the datacubes of the other two isotopologues.

4. Opacity and temperature structure of B59

4.1. CO-to-H_2 relation

The column density structure of B59 as seen with the dust extinction and emission is now relatively well known (Román-Zúñiga et al. 2009, 2012; Peretto et al. 2012). The dust extinction, contrary to the dust and gas emission, is not sensitive to the temperature. As such, studying the relation between the H_2 column densities derived from the dust extinction and the gas emission can give an insight to optical depth effects, temperature effects and the local abundance of that molecule with respect to H_2.

Figure 4 presents the relation between H_2 column densities and the ^{13}CO and $C^{18}O$ emission in B59 as scatter plots. The H_2 column density was derived from the extinction map of B59 (Román-Zúñiga et al. 2009) assuming $N(H_2)/A_v = 9.4 \times 10^{20}$ cm^{-2} mag^{-1} (e.g. Bohlin et al. 1978; Pineda et al. 2008). This was plotted against the ^{13}CO and $C^{18}O$ integrated intensities corrected for the telescope efficiency. Both the extinction and the molecular line maps had 20″ resolution and were resampled to a common area and pixel size, for a pixel-to-pixel comparison.

On the figure the coloured symbols indicate the correlation predicted by the non-LTE radiative transfer model RADEX (van der Tak et al. 2007) for different kinetic temperatures, using a volume density above the critical densities of ^{13}CO and $C^{18}O$ (3-2). The H_2 column densities are estimated assuming a fractional abundance of ^{13}CO and $C^{18}O$ with respect to H_2 of 1.4×10^{-6} and 1.7×10^{-7} respectively (Frerking et al. 1982). These models are only meant to illustrate the behaviour of the emission at different temperatures, and they do not represent actual fits to the data-points. The curves show the turn-over between a linear correlation between gas emission and H_2 column density and where the lines become optically thick. The linear portion of the curve is related to the abundance of ^{13}CO and $C^{18}O$ relative to H_2.

To estimate the masses and column densities directly from the gas emission (Appendix A), we estimate a "conversion" factor, X_{CO}, on the linear portion of the datapoints as X_{CO} =

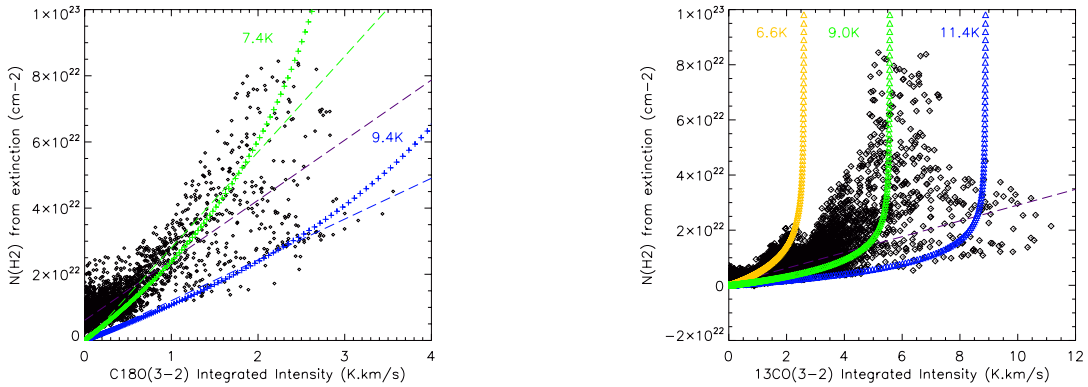

Fig. 4. Scatter plots of the H_2 column density retrieved from the extinction map against the $C^{18}O$ (left) and ^{13}CO (right) integrated intensity in units of T_{mb}, for each pixel in the map. The purple dashed-lines represent the linear fit of the data points, with an upper limit constraint on the column density for the case of ^{13}CO. Overlaid on the scatter plots are the predictions of RADEX models at different gas temperatures (on the left: 7.4 K in green and 9.4 K in blue crosses; on the right: 6.6 K in yellow, 9.0 K in green and 11.4 K in blue triangles). For the $C^{18}O$ (left) the green and blue dashed lines represent the linear approximations to the respective colour-coded RADEX model.

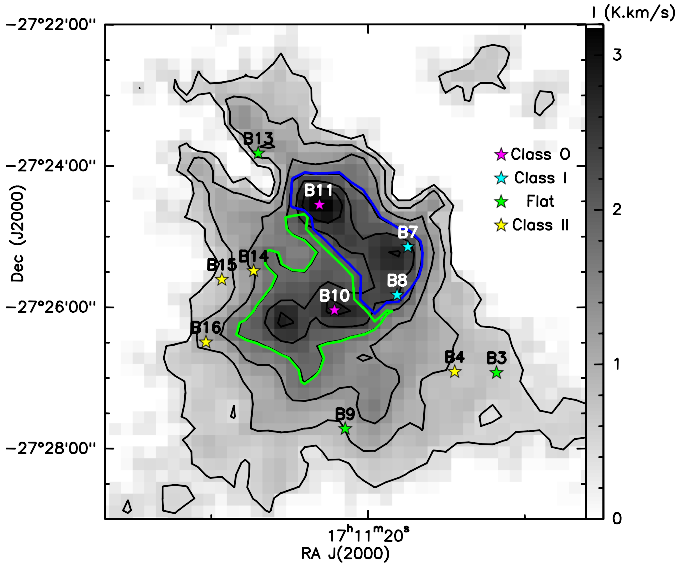

Fig. 5. Integrated intensity of $C^{18}O$ (3-2) in the central B59 (gray scale and contours). Protostars are marked with star symbols, and labeled as from Brooke et al. (2007). The green and blue contoured regions correspond to the regions identified from $C^{18}O$ scatter plot (see text and Fig. 4 left panel). They also correspond to the green and blue departures of the ^{13}CO integrated emission. Though adjacent, these two regions have a temperature difference of ∼2 K, the blue region being warmer. Note that while the colder green region hosts a single protostar (B10) and a "starless" $C^{18}O$ peak, the warmer blue region has three embedded protostellar objects (B11, B7 and B8).

$N(H_2)/I_{CO}$ (e.g. Pineda et al. 2008), where $N(H_2)$ is the H_2 column density and I_{CO} is the integrated intensity of the molecular transition.

For $C^{18}O$, a linear fit to all the data points provides a $X_{C^{18}O} = 1.82 \times 10^{22}$ cm^{-2}K^{-1}km^{-1}s (purple dashed line, Fig. 4 left panel), which will be used to estimate the masses on the bulk of the cloud. However, the points above and below the purple line, with $I_{C^{18}O} > 1.5$ K km s^{-1}, fall into two spatially distinct regions of B59 (Fig. 5, green and blue contoured regions respectively). These two regions are of particular interest on the optical depth and temperature structure. To better estimate the masses and virial parameters in these two specific regions, we used a linear fit to the green and blue models, for $N(H_2) < 8 \times 10^{22}$ cm^{-2} and $I_{C^{18}O} < 3$ K km s^{-1}, shown as blue and green dashed lines on Fig. 4 left panel. These correspond to a $X_{C^{18}O}$(green) $= 2.89 \times 10^{22}$ cm^{-2}K^{-1}km^{-1}s and $X_{C^{18}O}$(blue) $= 1.23 \times 10^{22}$ cm^{-2}K^{-1}km^{-1}s.

For ^{13}CO we estimated a $X_{^{13}CO} = 2.85 \times 10^{21}$ cm^{-2}K^{-1}km^{-1}s by constraining the linear fit to pixels where $N(H_2) < 3 \times 10^{22}$ cm^{-2} (purple dashed line on Fig. 4 right panel). We use this value to estimate the masses of the bulk of the cloud, but we note that it will only provide a lower limit in the regions that show significant departures from the linear trend due to optical thickening.

4.2. Optical depth of $C^{18}O$ and ^{13}CO

To measure the optical depth of the ^{13}CO and $C^{18}O$ and study its variation across the cloud, we have followed the method in Ladd et al. (1998). This uses the ratio of the integrated intensities, and assumes the same excitation temperature for both species. The method is quite insensitive to the line width assumed, and therefore we have adopted a velocity width of 1 kms^{-1} throughout.

The ratio map between the integrated intensities of ^{13}CO to $C^{18}O$ (not shown) has values ranging from 2 to 4 in the denser regions, and approaching 9 towards the edges of the cloud. A linear fit to the pixel-by-pixel comparison of the two species suggest a fractional abundance around 6.4. However this value is significantly affected by the denser regions where the ^{13}CO line becomes optically thick. Therefore, we adopt the fractional abundance of ^{13}CO with respect to $C^{18}O$, f, of 8.4 (Frerking et al. 1982), which is more consistent with the ratio we find at the edge of the cloud. This ratio implies $C^{18}O$ optical depths ranging from 0.1 to 0.5 over most of the cloud but ranging from 0.5 to 1.25 towards the central clump (Fig. 6), consistent with the expected increase of opacity from the $C^{18}O$ scatter plot. Therefore, we will consider $C^{18}O$ to be optically thin throughout the cloud, but only marginally so towards the central cores.

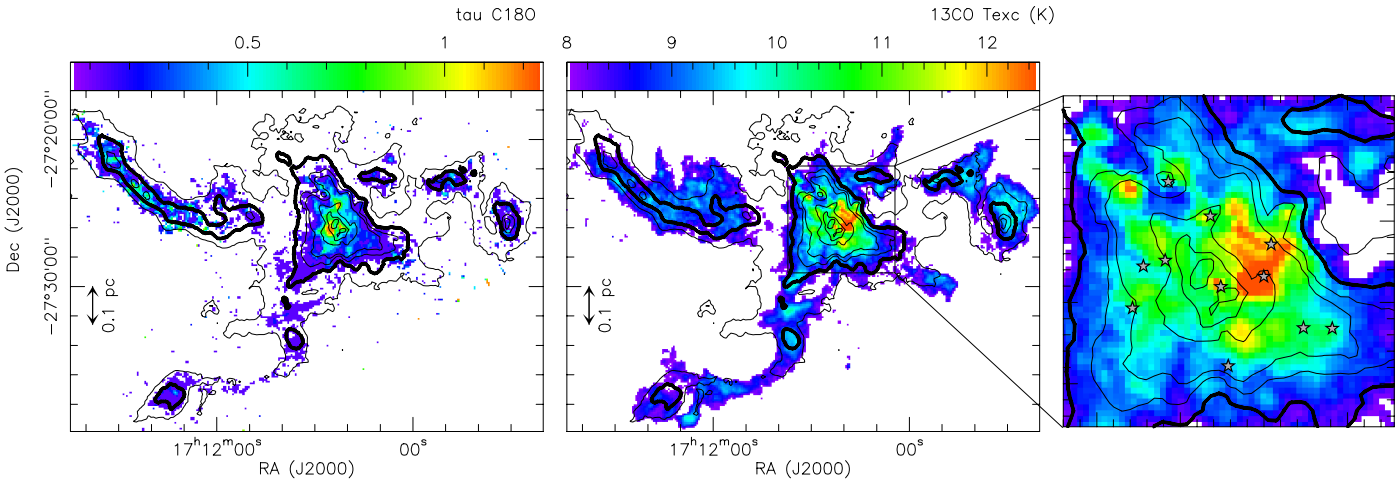

Fig. 6. *Left*: map of the $C^{18}O$ opacity in colour scale, calculated from the ratio of ^{13}CO to $C^{18}O$. The $C^{18}O$ optical depth is lower than 0.5 in most of the cloud, and only in the central B59 core it raises to higher values, with three local peaks where it reaches values around unity. *Centre and right*: ^{13}CO excitation temperature map in colour scale, showing an increase of temperature towards the central B59 (zoomed in on the right panel). In all panels, the contours are the dust extinction as in Fig. 1. The darker contour at an A_v of 10, delineates the regions most likely to be under LTE conditions.

4.3. Excitation temperature structure

Since the ^{13}CO peak emission is optically thick in the bulk of the cloud ($\tau_{13} > 1$), we estimate the excitation temperature of ^{13}CO assuming LTE conditions and optically thick emission. Using the radiative transfer equations under this assumption (e.g. Rybicki & Lightman 1986), we have the relation:

$$T_{\rm ex}(^{13}{\rm CO}_{3-2}) = \frac{15.87}{\ln[1 + 15.87/(T_{max}(^{13}{\rm CO}) + 0.045)]} \quad (1)$$

where 15.87 is $h\nu/k$ for the frequency of ^{13}CO $J = 3 \rightarrow 2$, where h is the Planck constant, ν is the frequency and k is the Boltzmann constant. Here, T_{max} is the peak main beam temperature of the line. When ^{13}CO presents a self absorption dip, the peak used corresponds to the absolute maximum of the emission.

The resulting excitation temperature map is shown in Fig. 6, where we can see that most of the cloud is at ~ 9 K, and the star forming core is at 10 - 12 K. Given that the ^{13}CO traces some of the outflow emission and the excitation temperature was estimated using the emission peak, in regions with self absorption we will be measuring the excitation temperature of the outflowing warmer gas. As such, these outflow shocks can be seen in this image as local temperature maxima, even outside the B59 central region (for instance in the SE U-shaped ridge). Outside the contoured region shown in Fig. 6 the temperatures decrease to as low as 5 K. However, in these ^{13}CO diffuse emission regions, not only it is likely that the ^{13}CO has lower optical depth, but also the densities are lower than the critical densities for LTE conditions, limiting the validity of this approach.

We can compare this temperature structure with what is predicted from the ^{13}CO scatter plots (right panel of Fig. 4). Firstly, we can identify three departures from the linear relation, explained by different gas temperatures (RADEX models in yellow, green and blue triangles). The first departure, at $I_{^{13}CO}$ = 2 K kms^{-1}, corresponds to the NE ridge of B59, and is consistent with very low temperatures (yellow triangles). Even though the RADEX predictions indicate temperatures below 7 K, the LTE estimate (Fig. 6) shows temperatures closer to 9 K.

The two other departures, one where $I_{^{13}CO} \sim 6$ K kms^{-1} and the other where $I_{^{13}CO}$ has its highest values, at column densities below 4×10^{22} cm^{-2}, correspond to the same two regions as those selected from the $C^{18}O$ scatter plot (contoured in Fig. 5). These are two adjacent portions in the central B59 region, each of them containing one of the two younger sources in the field (B10 and B11). We find that these two regions show a temperature difference of ~ 2 K with both molecules (green and blue models on Fig. 4). Note that the warmer (blue) region also includes another two more evolved protostars (B7 and B8). This temperature difference inside the central region is consistent with our LTE ^{13}CO excitation temperature estimate shown on Fig. 6. The increase of temperature in the central region is associated with the position of the protostars, and it is likely due to the combined heating effect from radiative and outflow feedback from these young sources. However, the importance of the radiative feedback in the temperature is felt only locally (within less than 10 000 AU from the protostars), and even though it could be important to change the fragmentation properties of the gas at these scales, it likely does not substantially alter the fragmentation at the scale of B59 star forming clump (i.e. ~0.3 pc).

5. Outflows

5.1. Identification of individual outflows

To identify the B59 population of protostellar outflows, and estimate both their global and individual physical properties and energetics, we made use of our ^{12}CO mapping observations. These reveal a number of outflows bursting from the central sources of B59. The left-hand panels of Fig. 7 show the larger scale outflows of B59 in the ^{12}CO blue and red emission. Here, we can see a relatively compact outflow emission bursting to the NE of the central region with both a red and blue lobe, spatially coincident (best seen on the right-hand panels of Fig. 7), and that fall in the extinction Cavity B (Fig. 1). This outflow appears to trace back to one of the youngest sources in the field (the Class 0/I source B11).

Another set of larger scale outflow features can be seen to the SE U-shaped ridge, including a series of blue knots, and a red arc, roughly towards the same direction. The zoom-in of the central region (right panels) show that the driving source of the outflow responsible for the southern blue knot seems to be the other young Class 0/I source in the field (source B10). On the

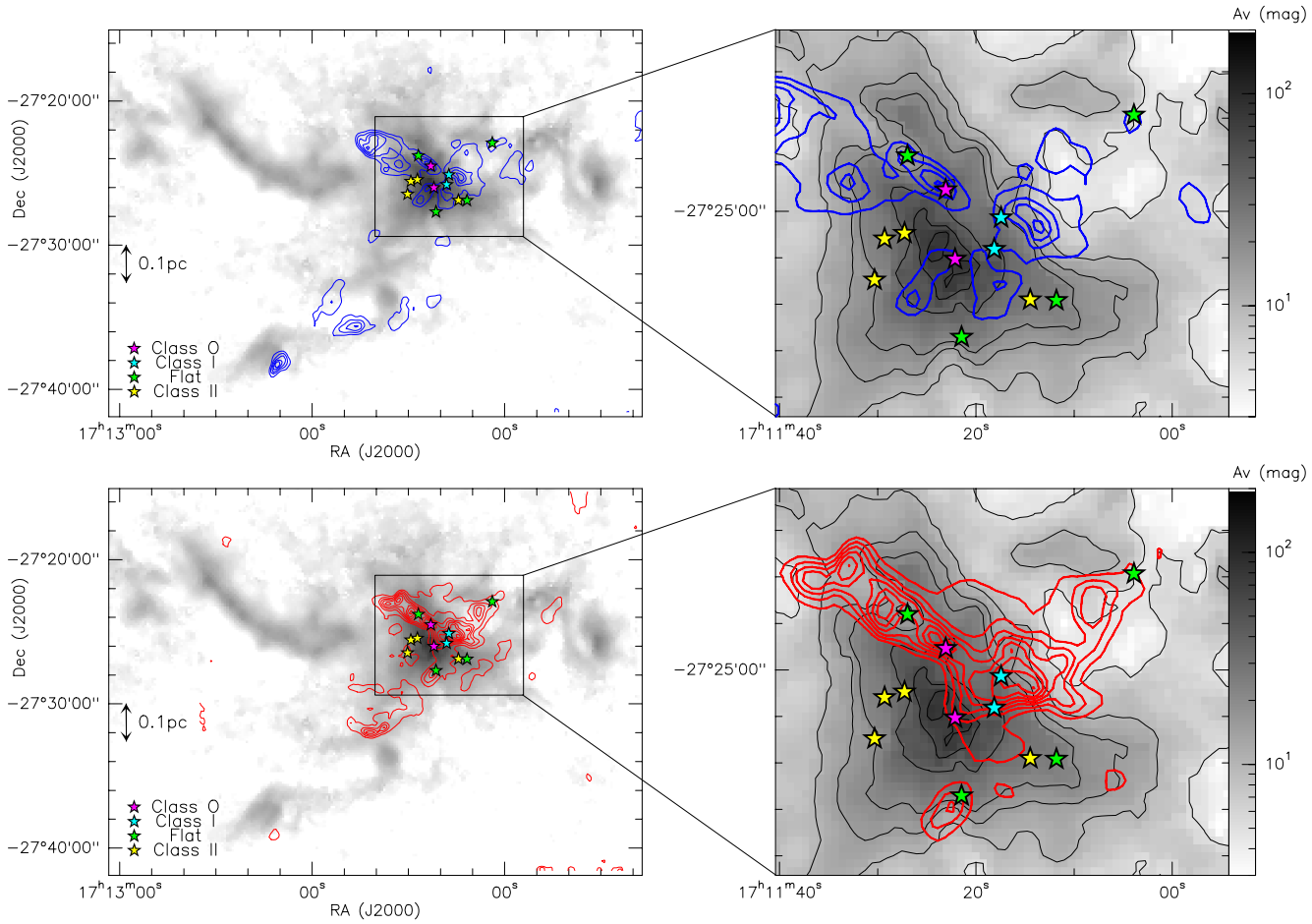

Fig. 7. ^{12}CO outflow emission in B59 as blue and red contours, with the YSOs positions, over-plotted on the extinction map from Fig. 1 in gray scale (and black contours on the right-hand panels). The left-hand panels show the high velocity emission in the entire B59, while the right panels show a zoom in the central star-forming core. The ^{12}CO emission was integrated from -5 to 2.7 kms^{-1} (blue) and from 4.2 to 15 kms^{-1} (red). The contours are from 3 K kms^{-1} on the left panels and from 4 K kms^{-1} on the right panels, in steps of 2 K kms^{-1}.

other hand, the red arc seems to be part of the outflow bursting from an older source (source B9).

This zoom-in also shows that the two Class I sources (B7 and B8 light blue stars) sit on a region where the ^{12}CO from the outflows of the two younger sources (purple stars) start to become confused. Therefore, despite the fact that some of the ^{12}CO wing emission in this particular region is likely to be driven by these two Class I sources, it is hard to disentangle it from the outflows from the other nearby protostars. Finally, the flat sources B1/B2 (the western-most green star) also seem to show some signs of outflow emission. Though not very high velocity nor very strong emission, these outflow lobes (in particular the red one) fall the dust Cavity C.

For many of these outflow features, we cannot clearly identify the second counterpart of the bipolar outflows. This is likely due to confusion of the more compact outflows in the central region. For this reason, in this paper we will focus on the properties of the unconfused individual outflows as well as on the global outflow properties. Interferometry data will be important in disentangling these compact outflows close to their driving sources, and better estimate the energy release.

5.2. Outflow inclination angles

Before estimating the momentum, momentum flux and energy of the outflows, the observed velocities need to be corrected for the outflow inclination angle i (i = 0° along the line of sight). Observationally, it is hard to infer the inclination angle of the outflows with precision, and this introduces a critical source of uncertainties, as the velocities (and momentum) will be affected by a factor of $1/cos(i)$, the energies, by a factor $1/cos^2(i)$, and the momentum flux, by a factor $sin(i)/cos^2(i)$.

Nevertheless, for a few particular outflows in B59, a careful comparison of the blue and red emission can shed some light on the overall inclination of the flows. In particular, Flow 1 (Fig 8), powered by B11, shows overlapping blue and red emission, consistent with being a single outflow lobe, close to the plane of the sky. Because the observed maximum velocities along the line of sight for the blue and red wings are simillar, this constrains the outflow axis to being in the plane of the sky to less than 5° uncertainty (i.e. otherwise the blue and red absolute velocities would differ by more than a factor 2). In addition, the projected opening angle of this outflow is of ∼30°, implying that each of the outflow cone walls are inclined by ∼15° with respect to the plane of the sky, giving $i \sim 75°$. Note that if the outflow axis changes by 5°, the inclination angles would change, but while one would increase to 80°, the other would decrease to 70°. Because the mass, extent and velocities of the two lobes are similar, doing so

Table 1. Outflow properties

	M ($M_\odot$)	p_{out} ($M_\odot$ kms^{-1})	p_{out}^{corr} ($M_\odot$ kms^{-1})	E_{out} ($M_\odot$ km^{2}s^{-2})	E_{out}^{corr} ($M_\odot$ km^{2}s^{-2})
Blue	0.59	0.83	3.21	0.81	12.1
Red	0.63	0.55	2.13	0.40	5.97

Table 2. Momentum flux of individual outflows

	Driving source	l (pc)	v_{max} (kms^{-1})	i (°)	l^{corr} (pc)	v_{max}^{corr} (kms^{-1})	t_d ($\times 10^3$ yr)	M ($M_\odot$)	p_{out}^{corr} ($M_\odot$ kms^{-1})	E_{out}^{corr} ($M_\odot$ km^{2}s^{-2})	F_{out}^{corr} ($M_\odot$ kms^{-1}yr^{-1})
Flow 1 - Blue	B11	0.19	-5.5	75	0.20	-21.3	9.2	0.15	0.97	4.36	1.1×10^{-4}
Flow 1 - Red	B11	0.11	5.0	75	0.11	19.3	5.6	0.14	0.65	2.89	1.2×10^{-4}
Flow 2 - Red	B9	0.23	5.5	57*	0.27	10.1	26.1	0.22	0.36	0.46	1.3×10^{-5}
Flow 3 - Blue	B10	0.45	-4.0	75	0.47	15.5	29.6	0.17	0.88	3.11	2.9×10^{-5}

* We adopt a correction factor of 2.9 for the momentum flux of Flow 2 (i.e. $i \approx 57°$), based on a random distribution of inclination angles (Cabrit & Bertout 1992; Bontemps et al. 1996), as it does not show a blue and red overlap, indicative of not being as close to the plane of the sky as Flows 1 and 3. If assuming 75°, the momentum flux of Flow 2 would increase by a factor 5.

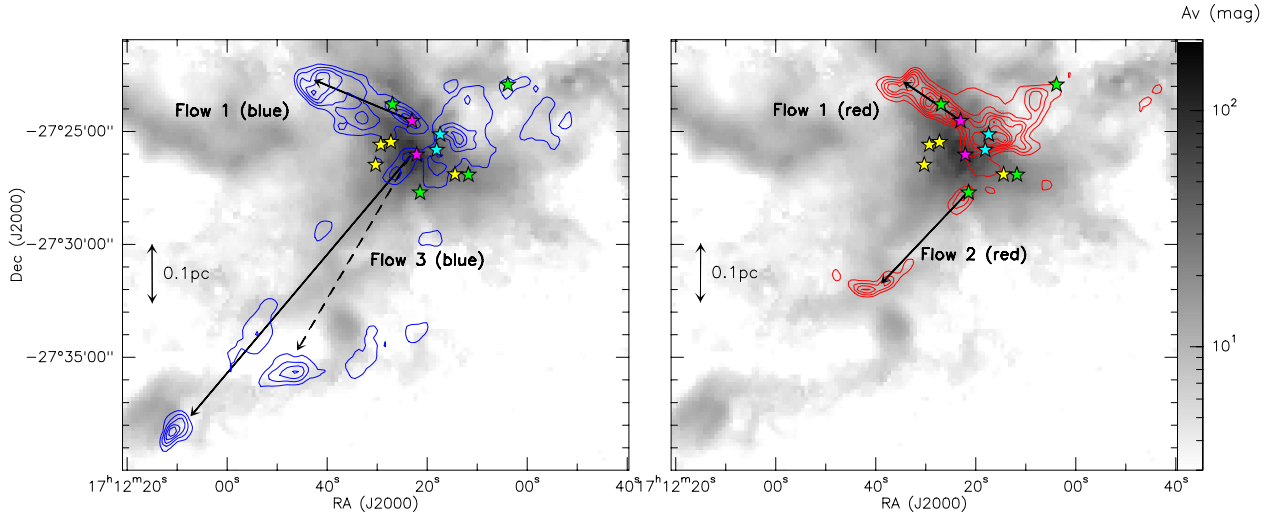

Fig. 8. Contours of the ^{12}CO blue and red emission (left and right panels respectively). Contours start at 3 K kms^{-1} for the blue emission and at 4 K kms^{-1} for the red, with steps of 2 K kms^{-1}, overlayed on the extinction map of B59 as from Fig. 1 in gray scale. The black arrows show the different individual outflows used to calculate individual outflow properties: Flow 1 (blue and red), Flow 2 (red) and Flow 3 (blue).

would in fact increase the estimate of the momentum and energy by a factor of 3. Therefore, $i \sim 75°$ for Flow 1, remains a rather conservative value.

For Flow 3, the large spatial extent of the collimated blue knot (with a faint red counterpart at the end), combined with a young driving source (B10) and a small velocity offset from the ambient cloud, also favours an outflow close to the plane of the sky. For simplicity, we will adopt the same inclination angle as for Flow 1. Considering the preferential alignment of the stronger outflows close to the plane of the sky, we also adopt $i \sim 75°$ to estimate the global outflow properties.

5.3. Outflow properties

To estimate the mass of high velocity gas in the outflows, the optical depth of ^{12}CO in the wings has to be corrected for. This can be done using the ^{13}CO data. Under LTE conditions and assuming similar excitation temperatures, a fractional abundance of ^{12}CO relative to ^{13}CO of 62 (Langer & Penzias 1993), and optically thin ^{13}CO wing emission (Cabrit & Bertout 1990), the optical depth of ^{12}CO (τ_{12}) can be determined from the ratio of the integrated wing emission of the two isotopologues. We integrated below 2.7 km s^{-1} for the blue wing and above 4.2 km s^{-1} for the red.

For each wing, we then apply the correction factor of $\tau_{12}/(1-e^{-\tau_{12}})$ for the column density estimate at each pixel (Cabrit & Bertout 1990; Curtis et al. 2010b) . Assuming a kinetic temperature of the outflows of 25 K (twice warmer than the dense gas), a CO abundance with respect to H_2 of 10^{-4} and for a distance of 130 pc, the gas masses can be derived as:

$$M = 1.78 \times 10^{-6} N_{pix} < \int T_{mb} dv > \quad (2)$$

where M is the gas mass in $M_\odot$ assuming a molecular weight of 2.33, N_{pix} is the number of pixels in the outflows, and $< \int T_{mb} dv >$ is the average integrated intensity, after the opacity correction of the T_{mb} at each pixel. If assuming a higher temperature for the outflows of 50 K (as found by, e.g. Hatchell et al. 1999), our mass estimate would increase by 20%.

To estimate the average momentum, p_{out}, and kinetic energy, E_{out}, of the outflows, as well as the individual outflow momentum flux ,F_{out}, we use

$$p_{out} = \int m(v)|v - v_0| dv \quad (3)$$

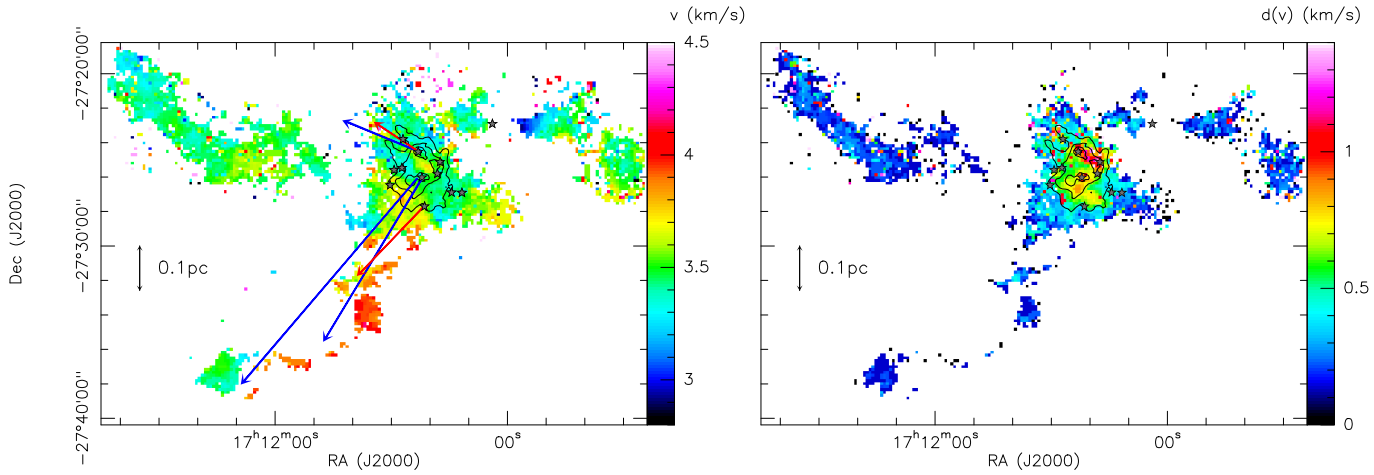

Fig. 9. $C^{18}O$ moment maps: mean velocity on the left panel, and velocity dispersion (FWHM) on the right, in colour scale overplotted with the integrated intensity in contours, and with the sources plotted as grey stars. The outflows identified on Fig. 8 are also plotted as blue and red arrows on the left-hand panel, for comparison to the local velocity fields.

$$E_{\rm out} = \frac{1}{2}\int m(v)(v - v_0)^2 dv. \quad (4)$$

$$F_{\rm out} = p_{\rm out}/t_d \quad (5)$$

where v_0 is the velocity of the driving source, $m(v)$ the mass corrected for the optical depth, and t_d is the dynamical time of the outflow, defined as $t_d = l/v_{\rm max}$, l being the length of the flow, and $v_{\rm max}$ the maximum velocity of that flow.

The global momentum and energy of the outflows are summarised on Table 1, where M is the gas mass contained in each of the outflow lobes, $p_{\rm out}$ is the momentum and $E_{\rm out}$ is the kinetic energy, shown here both without a correction for inclination angle, and also assuming an inclination angle of 75° ($p^{\rm corr}_{\rm out}$ and $E^{\rm corr}_{\rm out}$).

We then estimate the individual momentum flux for the four main flows of B59 (Fig 8). The results are shown in Table 2, where l is the projected length of the outflow in the plane of the sky, i is the assumed inclination angle, $v_{\rm max}$ is the line-of-sight maximum velocity with respect to the cloud's ambient velocity of 3.5 $\rm kms^{-1}$. The following columns present the remaining outflow properties as corrected for the inclination angle. The momentum flux of Flow 1 is higher than the momentum flux for Flow 2 and 3 and is consistent with the expected values for Class 0 sources (i.e. $\sim 10^{-4}$ $\rm M_\odot$ $\rm kms^{-1}yr^{-1}$, Bontemps et al. 1996; Curtis et al. 2010b) . Flows 2 and 3, however, have slightly lower momentum fluxes and start to approach those of a Class I protostar (i.e. $\sim 10^{-5}$ $\rm M_\odot$ $\rm kms^{-1}yr^{-1}$, Bontemps et al. 1996; Curtis et al. 2010b). Nevertheless, they are all between the expected values for Class 0 and I.

6. Ambient cloud

6.1. Dynamics

To study the dynamics of the ambient gas of B59, we use the combined information from all three CO isotopologues. With the $C^{18}O$ emission in particular, we investigate the velocity gradients and changes in the velocity dispersion across the region (Fig. 9).

The velocity map of the region (left panel of Fig. 9) shows that the NE ridge is uniform in velocity, at around 3.5 $\rm kms^{-1}$. Not only we find little variation on the velocities in this ridge, but also the linewidth is very small (with FWHM as low as 0.3 $\rm kms^{-1}$, right panel of Fig. 9).

The U-shaped ridge (Fig. 1) shows a more complex velocity structure, presenting higher velocities than the rest of the cloud (at around 4 $\rm kms^{-1}$). This is somewhat surprising, since this edge correlates with a blue outflow knot from Flow 3 (Fig. 7). This is consistent with an outflow close to the plane of the sky where the redshifted U-shape shows the compressed material behind the outflow, even though there are no signs for a linewidth broadening in this ridge (right panel of Fig. 9).

The red arc from Flow 2 is also correlated with a $C^{18}O$ and extinction arc, delineating the right hand side of the U-shape. This $C^{18}O$ gas has higher velocities than the centre of B59, consistent with being pushed by the red-shifted Flow 2 which has a more important inclination with respect to the plane of the sky.

In the central clump of B59 there is a velocity gradient of about 1 $\rm kms^{-1}$ across 0.1 pc (left panel of Fig. 9). There is also a local increase of the linewidth, with the velocity dispersion (FWHM) ranging from 0.5 $\rm kms^{-1}$ to 1.2 $\rm kms^{-1}$.

This increase of linewidth can also be seen through position-velocity (PV) diagrams (Fig. 10 and 11). The PV 1 slices the datacube along the axis of Flows 2 and 3. On the left panels of Fig. 11 we can see the blue and red outflow knots from Flow 3 at ∼2.1′ offset as well as the red knot of Flow 2 at ∼11.5′ offset, in ^{12}CO and ^{13}CO. The velocity structure of the U-shaped ridge is seen from 3′ to 14′ offsets where, while the eastern end is described by velocities ∼3.2 $\rm kms^{-1}$, the U-shaped and western end have stronger emission at ∼4 $\rm kms^{-1}$ (cf. Fig. 9). The ^{13}CO traces these two velocities throughout the ridge, but in fact, the U-shape itself is correlated with the red component (centre-left panel of Fig. 10). The cavity A is therefore also seen as a cavity in the ^{13}CO (low-velocity) red emission. The central region of B59 is delimited with a sharp edge (at an offset of 20.5′), where the emission from $C^{18}O$ is broad, and after which the emission drops out sharply to noise levels (in Cavity C). This cavity, seen in extinction and with both ^{13}CO and $C^{18}O$, is delimited on both sides with high velocity outflowing gas.

The right column of Fig. 11 shows the PV 2 which cuts through the NE ridge of B59 (from 1′ to 12′ offset), confirming its small linewidths and constant velocity throughout. The emission from the central portion of B59 is seen with offsets between 14′ and 20′ and, similarly to PV 1, it is delimited by a sharp edge to the west (leading onto the same Cavity C as that seen on PV

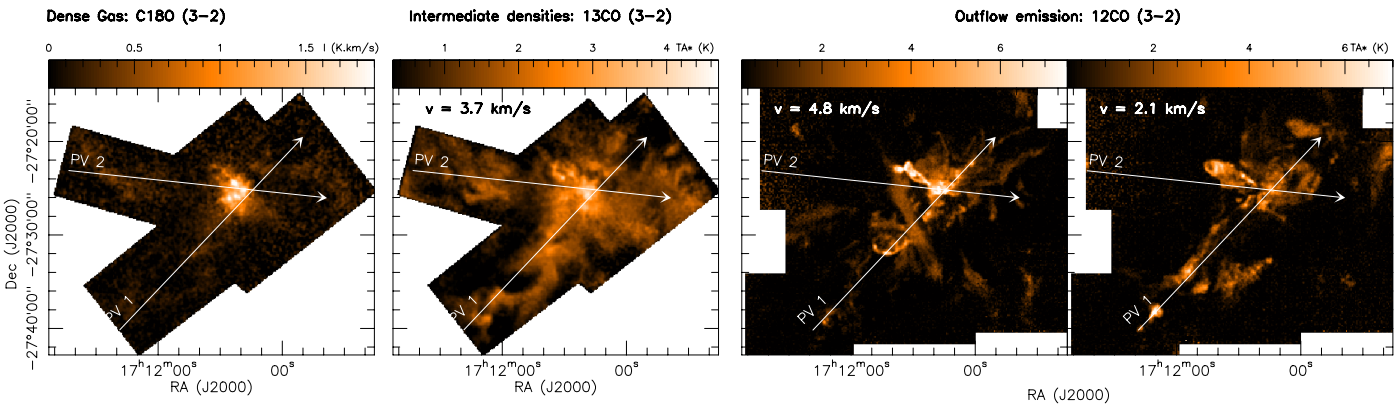

Fig. 10. Left: Integrated intensity map of $C^{18}O$ (in units of T_A^*) showing the distribution of the dense gas in B59; Centre-left: ^{13}CO channel map at v = 3.7 kms^{-1} (slightly red-shifted with respect to the cloud's ambient velocities of 3.5 kms^{-1}), tracing the intermediate density gas, and showing some of the cavities discussed in the text; Centre-right and Right: ^{12}CO channel maps at v = 4.8 kms^{-1} and v = 2.1 kms^{-1} respectively, illustrating the red and blue outflows of the region. The position of the two position-velocity diagrams of Fig. 11 are shown as white arrows and labeled as PV 1 and PV 2 in the four panels.

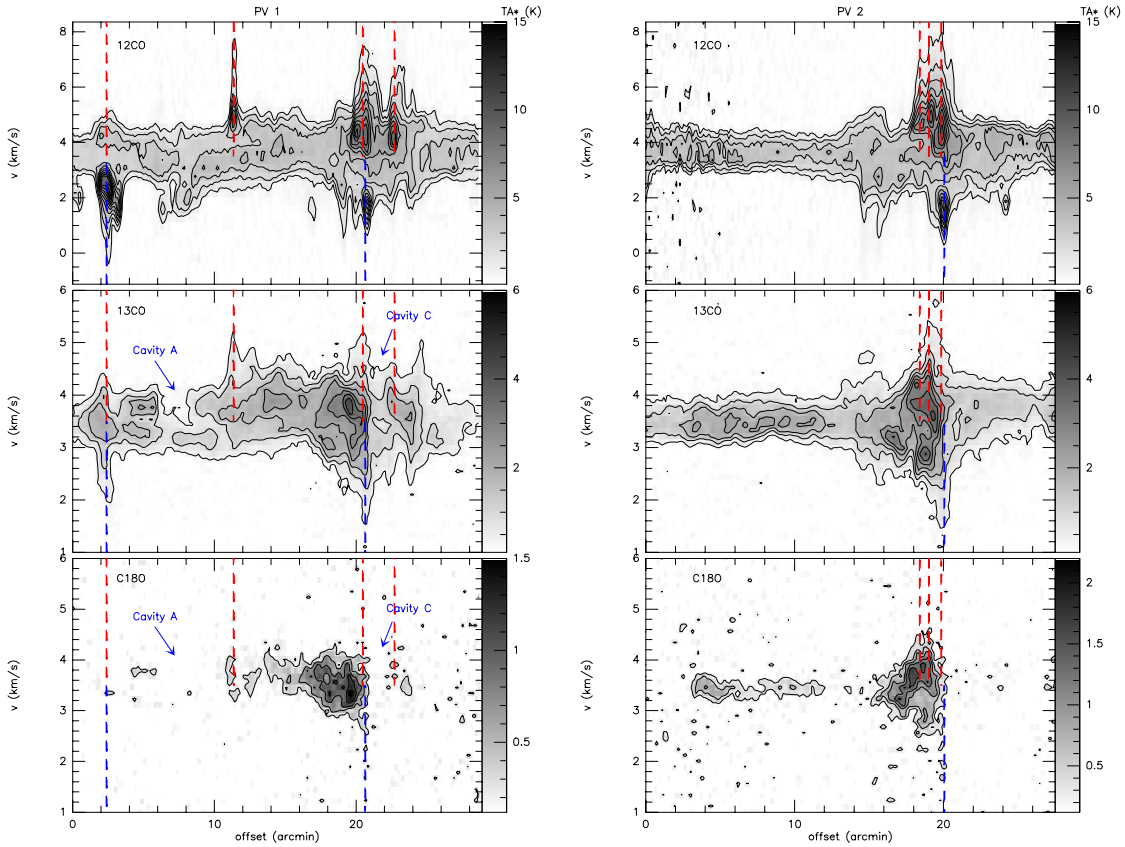

Fig. 11. Two PV diagrams of B59 in ^{12}CO (top panels), ^{13}CO (centre) and $C^{18}O$ (lower panels). Each column is the PV cut as labeled at the top and as shown in Fig. 10. The position of some of the outflows are put in evidence with the blue and red dashed lines and a cavities is also pointed and labeled. Contours are from 1 K with steps of 1 K for ^{12}CO, from 0.3 K with steps of 0.6 K for ^{13}CO and from 0.25 K with steps of 0.3 K for $C^{18}O$ (in T_A^*).

1). The $C^{18}O$ emission shows significant local broadening and the velocities agree to those of ^{13}CO. In particular, the red outflow wings pointed out correlate with regions where the $C^{18}O$ is broader with a stronger red emission. The marked blue outflow wing can be tentatively seen with $C^{18}O$ but it approaches the noise level of the data. Nevertheless, the (lower velocity) blue ^{13}CO emission at an offset of ∼20′ is also seen in the $C^{18}O$ PV diagram.

6.2. The hierarchical structure

To study the hierarchical structure of B59, we have used a dendrogram extraction technique, developed by Rosolowsky et al. (2008). This analysis is useful to understand the different structures that lie within B59. However, like any other clump-extraction code, it cannot be used blindly in a region. In the case of B59, most of the leaves retrieved are not "real" cores - in the sense of structures which are progenitors of future or

currently forming protostars. In fact, only two leaves in the central B59 correspond to actual star-forming cores. The remaining structures trace the two-halves of outflow emission, or less dense material which may or may not be bound to form stars in the future. A detailed description of the analysis and results from this extraction can be found in Appendix A, and they confirm the broken structure of B59. In summary:

- The SE U-shaped ridge is not a single structure but two different arch-like gas, consistent with two compressed fronts from two different outflows (Flows 2 and 3). This suggests that the gas once in Cavity A has, in fact, been cleared by Flow 3 and compressed onto forming the eastern side of the U-shaped ridge.
- The Western cores are physically separated from the main B59 structure, consistent with the existence of a deep gas-deprived cavity (Cavity C). The presence of outflowing gas possibly associated with the B1/B2 system, which is seen in the edges of this cavity suggests that this cavity was possibly cleared by the outflow itself during earlier times of the evolution of these sources.
- The NE ridge is, at present, a non-sub-structured region, gravitationally bound, velocity-coherent, and with low velocity dispersion. It could possibly be on the verge of forming future prestellar cores;
- And finally, the dendrogram analysis finds that the central region does not show evidence for further fragmentation into new cores, apart from the two cores surrounding the younger protostars in the field. All the other structures found in this central region are part of outflowing gas, particularly along the walls of Flow 1.

7. Discussion: Outflows Interaction

7.1. Outflows and the Cloud

Our hierarchical study of the region also provides a reliable mass estimate throughout the different scales of the cloud, which can be used to estimate the binding energy at different scales. In particular, under the hypothesis that outflows are important in B59, their impact in the cloud can be estimated by comparing the kinetic energy carried out by the outflows and the binding energy of the denser material. The total kinetic energy of the outflows (Sect. 5) is $\sim$18 $M_\odot$ km^{2}s^{-2}, when assuming an inclination angle of 75° for the outflows. We estimate the binding energy (i.e. the potential energy) of the dense material using the $C^{18}O$ masses. For 30 $M_\odot$ and a radius of 0.30 pc (Appendix A), and assuming a density profile as $\rho \propto r^{-2}$ (similar to that found by Román-Zúñiga et al. 2012), the gravitational potential energy is 12 $M_\odot$ km^{2}s^{-2}, lower than the kinetic energy of the outflows. This means that the outflows carry an energy comparable to the binding energy of the dense material. However, we have to account for the fact that the kinetic energy of the outflows may be deposited outside the cores, and therefore may not be disrupting the dense cores themselves.

In fact, our study of B59 has shown that the outflows are correlated to the shapes and cavities seen in $C^{18}O$ and extinction outside the central region, indicating that these able to push, carve and shape the material (e.g. Sect. 6). This is the case, for instance, of the material along the SE U-shaped ridge, which is in fact a fossil of Flows 2 and 3. Its U-shape, its velocity structure, and its local temperature maxima are a result of the impact of outflows on an originally less dense medium.

7.2. Outflows and the Dense Gas

Despite the impact of the outflows in the B59 cloud at large scales, their importance on the dense gas is a bit harder to disentangle. For instance, in the denser central region of B59, we see temperature peaks likely due to a combined effect of the radiation from the individual protostars and the outflow shocks from the ensemble of the four protostars (Fig. 6). Furthermore, we detect a broadening of the $C^{18}O$ emission towards the central clump, which could be associated with a combination of rotation, shear, infall and outflow motions. An upper limit for the contribution of infall to the linewidth can be estimated by assuming that the entire B59 central clump is in free fall collapse. This would result on an infall velocity of $\sim 0.2-0.3$ km s^{-1} (generating a velocity dispersion of that order or less).

In specific regions, this broadening seems well correlated with the outflow wings from ^{13}CO (e.g. Sect. 6). To investigate more closely the local effects of the outflows on the dense gas we have studied the emission in an area where there was an initial evidence for the interaction of the outflow with the dense gas (with the existence of a cavity) and where no significant velocity gradients are present. This is the case along Flow 1, which is an unconfused and well collimated outflow located in the densest part of B59 (see Fig. 7). For this test case, we have compared the average profiles of the ^{12}CO integrated intensity as a measure of the outflow strength/position; the visual extinction as a measure of the quantity of material along the line of sight; and the $C^{18}O$ linewidth as a measure of the velocity dispersion. To do that, we took several slices along a perpendicular direction to the outflow main axis.

Since the outflow profile changes along its length, we estimated the average profiles within two separate regions. These are shown as boxes in Fig. 12 (left panels) overplotted on a close up of the central region of B59 in the ^{12}CO integrated intensity (top), the extinction map (middle) and the $C^{18}O$ linewidth (bottom). These boxes are colour-coded as the respective profiles, shown in the other panels of the same figure. To serve as reference, the dashed lines show the position of the peak of ^{12}CO integrated intensity.

Closest to the driving source, inside the blue boxed region, the outflow is collimated and constrained to a $\sim$1'-wide region (top row, central panel of Fig. 12). In the second region, delimited by the green box, outflow is broader (top row, right panel). Here, the blue emission starts forming an arched lobe opening towards the east (left-hand side), while the the red outflow ends with a sharp edge (c.f. Fig. 7 and 8). This sharp tip is immediately followed by a linewidth peak, reminiscent of an impacted outflow knot (Fig. 12, first column, lower panel).

In both boxes, the outflow falls in a similar-sized cavity in the extinction (middle panels). Just by looking at Fig. 7 (left panels), we already see that Flow 1 has interacted with its surrounding dense gas. Cavity B (cf Fig. 1) has clearly been cleared up by the this powerful outflow. Figure 12 bottom row shows the impact of such outflow on the dense gas velocity dispersion. Despite the $C^{18}O$ emission following a similar shape as the extinction (resulting on less $C^{18}O$ gas in this cavity), there is still enough material to detect an increase of linewidth along the outflow axis (lower row panels). Immediately before and after the outflow axis, towards higher column densities, the linewidths are still relatively high (when compared to the outer parts of B59), but decrease steadily as moving away from the outflowing material. This is the case of the regions in the green box between 1′ and 3′, where the $C^{18}O$ linewidth decreases until it reaches our detection limit. This suggests that the outflows are having a direct impact

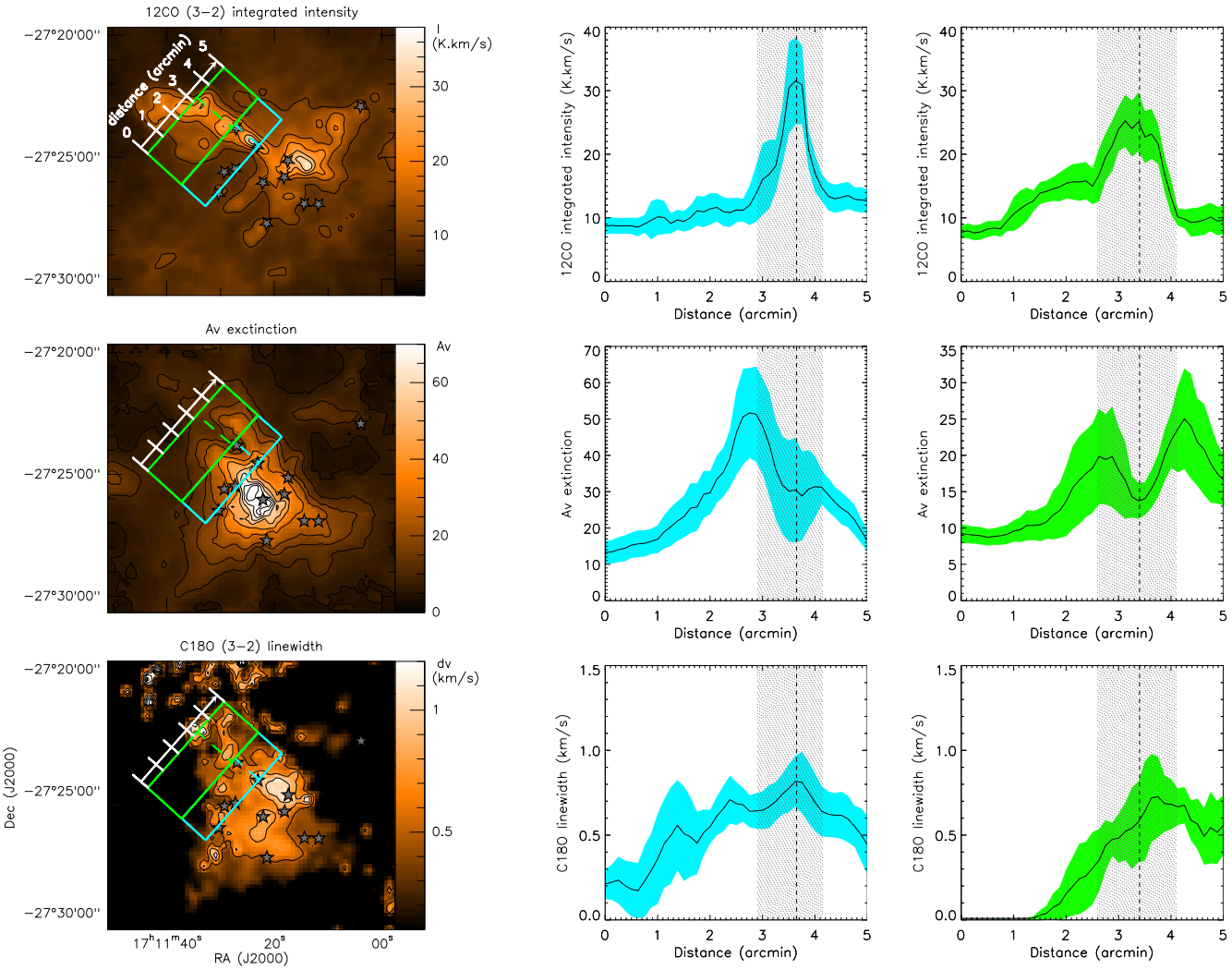

Fig. 12. *Left column*: close up of the central region of B59, where the colour scale and contours are the ^{12}CO integrated intensity map (top), the visual extinction map (centre) and the C^{18}O linewidth map (bottom). The regions used to estimate the average profiles (shown on the centre and right columns) across the Flow 1 are shown as blue and green boxes. The dashed lines show the position of the peak of ^{12}CO integrated intensity as averaged within each box. *Centre and Right columns*: average profiles of ^{12}CO integrated intensity (top row panels), visual extinction (central row panels), and C^{18}O linewidth (FWHM, bottom row panels). Each column corresponds to a different averaging box, colour-coded as in the left column. The dashed lines and gray-shadowed areas mark the peak and extent of the ^{12}CO profile as seen on the first row panels, respectively. The colour-coded shadowed areas show the 1-sigma dispersion of each quantity.

on both the shape of the region, and the linewidths of the denser material in B59.

To estimate an upper limit for the contribution from the outflow-generated turbulence in the total velocity dispersion of the region, we have assumed that the initial turbulence of the gas in B59 (before any outflow feedback) was as low as that currently found outside the central B59 (0.3 km s^{-1} FWHM in the NE ridge, cf. Fig. 9, and Tables A.1 and A.2), and that the increase of linewidth along Flow 1 is uniquely due to the outflow-injected turbulence. The maximum FWHM detected along Flow 1 is $\sim$ 1.0 km s^{-1}, so we estimate that the outflow-generated turbulence in B59 is locally of the order of 0.9 km s^{-1} FWHM (i.e. $\sigma_v^{out} \sim 0.4$ km s^{-1}). We stress, however, that this is most certainly dependent on the power of the outflow and on the age and mass of the driving source.

As another way to assess the importance of the outflows as turbulence generators, we have estimated the kinetic energy and compared that to the outflow energy (similarly to e.g. Arce et al. 2010). On the central region, the kinetic energy is $E_{\rm turb} = 4$ M$_\odot$ km^{2}s^{-2}, while the outflow energy, estimated on the same area is $E_{\rm out} = 0.62$ M$_\odot$ km^{2}s^{-2}, before applying any correction factor for the outflow inclination. If correcting for a random distribution of angles (i.e. $i \sim 57°$), this becomes $E_{\rm out}^{\rm corr} = 5.2$ M$_\odot$ km^{2}s^{-2}, or even $E_{\rm out}^{\rm corr} = 9.2$ M$_\odot$ km^{2}s^{-2} if assuming an inclination angle of 75° as in Sect. 5. This suggests that the outflows carry more than enough energy to provide the turbulent support of the central B59. However, since the central region of B59 presents some velocity gradients and is also likely more affected by infall motions, it is not trivial to conclude if the observed turbulence is dominantly due to the outflows injection.

We have circumvented this problem by estimating the fraction of the outflow energy deposited in the immediate surroundings of Flow 1. Taking the regions in the outflow walls we estimate, from the C^{18}O, that the total kinetic energy is of $E_{\rm turb} = 0.9$ M$_\odot$ km^{2}s^{-2}. From the respective portion of Flow 1, we estimate that the outflow energy is $E_{\rm out}^{\rm corr} = 2$ M$_\odot$ km^{2}s^{-2}. As men-

tioned in Sect. 5 a change in the inclination angle adopted for Flow 1 will increase the outflow energy estimate. This together with the fact that the total kinetic energy around the outflow does include other non-dominating terms (such as the thermal and isotropic turbulence), suggests that only a fraction (less than half) of the energy carried by the outflow is deposited in the immediate surroundings (consistent with, e. g. Cunningham et al. 2006). The remaining energy is deposited outside the star forming core.

We stress that this is valid for the specific case of Flow 1. This efficiency of outflow energy deposition will likely vary depending on the energy of the outflows and the density and velocity conditions of the regions with which the outflows interact.

8. Summary and conclusions

B59 is a star forming region with a small and young proto-cluster in its centre. Around it, only a few regions could be prone to collapsing in the future. One such region is the gravitationally bound NE ridge, that presents a coherent velocity structure, but that shows very little sub-structure at present times. Another region is one of the western cores, but whose mass reservoir available is not very significant. If becoming active, it will likely not form more than a single low mass protostar/protostellar system.

All the protostars are located in a $C^{18}O$ twisted filament-like structure (not seen in the dust) in B59's centre. In this region, there is a sharp temperature increase of 2K correlated with the position of the protostars, likely due to the protostellar radiative heating and outflow feedback. Nevertheless, we find the radiative heating to have a very localised effect, not likely to substantially change the properties of the fragmentation of B59 as a whole.

We identify a number of cavities in the ensemble of the B59 region, that show up either correlated with outflowing gas, or adjacent to outflow knots. Finally, we investigated the relation between the outflowing gas and the line width of the denser gas and found a clear correlation with an increase of linewidth of $C^{18}O$ along the outflow axis.

Our study of B59 suggests that the outflows are responsible for sweeping up and compressing the gas as they make their way out of the cloud. We conclude that the outflows are interacting closely with the dense material provoking a line broadening on the densest gas. When outside of the star-forming core, and as these outflows travel through a lower density material, their impact is seen as a re-shaping of the gas and dust that surrounds the protocluster. Their impact in the dense gas is shown to be an efficient source of turbulence that provides just enough support of the cloud against collapse at sub-parsec scales ($\sim$ 0.1-0.3 pc). The comparable kinetic and potential energy sustain the idea that the B59 core is long-lived and slowly collapsing. We, therefore, confirm that outflows are, as speculated by Covey et al. (2010) and Román-Zúñiga et al. (2012), the possible mechanism responsible for supporting the B59 clump against collapse.

A localised line broadening of the dense material is not commonly observed, since $C^{18}O$ does not trace high velocity outflowing gas. It may be so in B59 as most of the gas had originally narrow line widths, and any turbulence input due to outflows is more easily detected. In this context, B59 appears in marked contrast with regions such as Serpens (e.g. Duarte-Cabral et al. 2010), where no clear evidence for the outflows is seen in the $C^{18}O$ emission. Nevertheless, the actual linewidths of $C^{18}O$ in Serpens (homogeneously around $\sim$ 1-1.5 km s^{-1} FWHM) are in fact similar to those in the central core of B59. Serpens being a much more dynamic region (resulting from a collision of clouds, Duarte-Cabral et al. 2011) and with a large number of protostars powering outflows (more than 20 Class 0 and Class I sources in Serpens against four in B59), it may be that we are simply no longer able to detect the underlying quiescent gas of Serpens.

We suggest that outflows are an important means of inputting and sustaining turbulence in the surrounding gas, in agreement with the modeling work from e.g. Matzner (2007); Nakamura & Li (2007). However, in regions where the initial dynamics of the gas implies intrinsically larger linewidths, then the contribution from the outflow-generated turbulence can potentially become negligible. In fact, the final linewidth will only show a measurable broadening from the outflow contribution (of at least 30%), when the injected turbulence is at least as large as the original initial turbulence of the gas. Assuming that the measured generated turbulence ($\sigma_v^{out} \sim 0.4$ km s^{-1}) is close to the typical value of Class 0 protostellar outflows, the outflow broadening will only be detectable in regions where the original σ_v of the gas is of the order of 0.4 km s^{-1}. The relative support provided by such a turbulence input will also vary depending on the mass and the potential energy available to a given protocluster. In star-forming clumps embedded in more massive molecular clouds (i.e. lying in a deeper potential well), the gravitational energy will easily override such outflow-induced turbulent support, and the later will not be enough to halt a larger scale collapse.

We find that the energy carried by the outflows is larger than that needed to provide the current turbulent support of B59, and that only a fraction, less than half, of the energy of the outflows is efficiently converted into turbulent motions of the gas in the immediate surroundings of the outflows. The remaining energy is, therefore, deposited outside the star forming core. In regions denser than B59 this efficiency may increase, as the interaction of the outflowing gas and the environment will be more important. On the other hand, the balance of gravitational and turbulent energy will also be more important in such denser regions.

Acknowledgements. We thank J. Pineda and E. Rosolowsky for the support with using the dendrogram code. ADC is supported by the project PROBeS funded by the French National Research Agency (ANR). ADC also acknowledges the support of a grant from the Fundação para a Ciência e a Tecnologia (FCT) de Portugal, under which part of this work was achieved. The data reduction and analysis was done using the GILDAS software (http://www.iram.fr/IRAMFR/GILDAS) and the Starlink software (http://starlink.jach.hawaii.edu/starlink).

References

Alves, F. O. & Franco, G. A. P. 2007, A&A, 470, 597
Alves, F. O., Franco, G. A. P., & Girart, J. M. 2008, A&A, 486, L13
Arce, H. G., Borkin, M. A., Goodman, A. A., Pineda, J. E., & Halle, M. W. 2010, ApJ, 715, 1170
Arce, H. G. & Sargent, A. I. 2006, ApJ, 646, 1070
Bohlin, R. C., Savage, B. D., & Drake, J. F. 1978, ApJ, 224, 132
Bontemps, S., Andre, P., Terebey, S., & Cabrit, S. 1996, A&A, 311, 858
Brooke, T. Y., Huard, T. L., Bourke, T. L., et al. 2007, ApJ, 655, 364
Buckle, J. V., Hills, R. E., Smith, H., et al. 2009, MNRAS, 399, 1026
Cabrit, S. & Bertout, C. 1990, ApJ, 348, 530
Cabrit, S. & Bertout, C. 1992, A&A, 261, 274
Carroll, J. J., Frank, A., & Blackman, E. G. 2010, ApJ, 722, 145
Carroll, J. J., Frank, A., Blackman, E. G., Cunningham, A. J., & Quillen, A. C. 2009, ApJ, 695, 1376
Covey, K. R., Lada, C. J., Román-Zúñiga, C., et al. 2010, ApJ, 722, 971
Cunningham, A. J., Frank, A., & Blackman, E. G. 2006, ApJ, 646, 1059
Curtis, E. I., Richer, J. S., & Buckle, J. V. 2010a, MNRAS, 401, 455
Curtis, E. I., Richer, J. S., Swift, J. J., & Williams, J. P. 2010b, MNRAS, 408, 1516
Duarte-Cabral, A., Dobbs, C. L., Peretto, N., & Fuller, G. A. 2011, A&A, 528, A50+
Duarte-Cabral, A., Fuller, G. A., Peretto, N., et al. 2010, A&A, 519, A27+
Forbrich, J., Lada, C. J., Muench, A. A., Alves, J., & Lombardi, M. 2009, ApJ, 704, 292

Forbrich, J., Posselt, B., Covey, K. R., & Lada, C. J. 2010, ApJ, 719, 691
Frau, P., Girart, J. M., & Beltrán, M. T. 2012, A&A, 537, L9
Frau, P., Girart, J. M., Beltrán, M. T., et al. 2010, ApJ, 723, 1665
Frerking, M. A., Langer, W. D., & Wilson, R. W. 1982, ApJ, 262, 590
Fuller, G. A. & Ladd, E. F. 2002, ApJ, 573, 699
Hatchell, J., Fuller, G. A., & Ladd, E. F. 1999, A&A, 344, 687
Heitsch, F., Ballesteros-Paredes, J., & Hartmann, L. 2009, ApJ, 704, 1735
Hennebelle, P. & Chabrier, G. 2011, in IAU Symposium, Vol. 270, IAU Symposium, ed. J. Alves, B. G. Elmegreen, J. M. Girart, & V. Trimble, 159–168
Ladd, E. F., Fuller, G. A., & Deane, J. R. 1998, ApJ, 495, 871
Langer, W. D. & Penzias, A. A. 1993, ApJ, 408, 539
Lombardi, M., Alves, J., & Lada, C. J. 2006, A&A, 454, 781
Matzner, C. D. 2007, ApJ, 659, 1394
Matzner, C. D. & McKee, C. F. 2000, ApJ, 545, 364
Maury, A. J., André, P., & Li, Z.-Y. 2009, A&A, 499, 175
McKee, C. F. & Ostriker, E. C. 2007, ARA&A, 45, 565
Muench, A. A., Lada, C. J., Rathborne, J. M., Alves, J. F., & Lombardi, M. 2007, ApJ, 671, 1820
Nakamura, F. & Li, Z. 2008, ApJ, 687, 354
Nakamura, F. & Li, Z.-Y. 2007, ApJ, 662, 395
Nakamura, F., Sugitani, K., Shimajiri, Y., et al. 2011, ApJ, 737, 56
Onishi, T., Kawamura, A., Abe, R., et al. 1999, PASJ, 51, 871
Peretto, N., Andre, P., Konyves, V., et al. 2012, ArXiv e-prints
Pineda, J. E., Caselli, P., & Goodman, A. A. 2008, ApJ, 679, 481
Rathborne, J. M., Lada, C. J., Muench, A. A., Alves, J. F., & Lombardi, M. 2008, ApJS, 174, 396
Riaz, B., Martín, E. L., Bouy, H., & Tata, R. 2009, ApJ, 700, 1541
Román-Zúñiga, C. G., Alves, J. F., Lada, C. J., & Lombardi, M. 2010, ApJ, 725, 2232
Román-Zúñiga, C. G., Frau, P., Girart, J. M., & Alves, J. F. 2012, ArXiv e-prints
Román-Zúñiga, C. G., Lada, C. J., & Alves, J. F. 2009, ApJ, 704, 183
Rosolowsky, E. W., Pineda, J. E., Kauffmann, J., & Goodman, A. A. 2008, ApJ, 679, 1338
Rybicki, G. B. & Lightman, A. P. 1986, Radiative Processes in Astrophysics
Schneider, N., Csengeri, T., Bontemps, S., et al. 2010, A&A, 520, A49+
van der Tak, F. F. S., Black, J. H., Schöier, F. L., Jansen, D. J., & van Dishoeck, E. F. 2007, A&A, 468, 627
Vazquez-Semadeni, E. 2010, ArXiv e-prints
Vázquez-Semadeni, E., Gómez, G. C., Jappsen, A. K., et al. 2007, ApJ, 657, 870

Appendix A: The hierarchical structure of B59

A.1. Method: Dendrograms

To study the cloud structure of B59, we used a dendrogram code that accounts for the hierarchical structure of the cloud. It provides a tree-like structure of the cloud, and has been developed and applied to star forming regions by Rosolowsky et al. (2008). This technique begins with the identification of all local maxima on a datacube (the *leaves* of the tree-like structure), and contours down the dataset, finding all the underlying structure that connects the different leaves together (i.e. the *branches*), down to the *root*. Each connecting point between two structures (leaves, branches and root) is identified as a *node* in the tree. The code we used to implement this dendrogram technique is fully described in Rosolowsky et al. (2008). This code also calculates several properties of the cloud at each contour level, such as the integrated intensity, the size of the structure, the velocity dispersion, the mean velocity and mean position.

We can retrieve the mass by taking the linear relation between the H_2 column density and the integrated intensity of the molecular line considered ($X_{\rm CO}$). The masses are calculated within the code, following the procedure described in Rosolowsky et al. (2008), where:

$$M_{\rm CO} = 1.84 \times 10^{-20} X_{\rm CO} L_{\rm CO} \quad \text{(A.1)}$$

where $M_{\rm CO}$ is the H_2 gas mass (in $M_\odot$) derived from the CO isotopologue in consideration, $X_{\rm CO}$ is the CO-to-H_2 conversion factor described in § 4.1 (in units of $\rm cm^{-2}K^{-1}km^{-1}s$), and $L_{\rm CO}$ is the luminosity from the considered CO emission (in K km $\rm s^{-1}pc^2$). This luminosity $L_{\rm CO}$ is calculated as $L = Fd^2$, where d is the distance to the cloud and F is the integrated flux of the region, i.e. the sum of all the emission in the region, calculated as $F = \sum_i T_i\, \delta\theta_x \delta\theta_y\, \delta v$. The value of 1.84×10^{-20} arises from the units conversion, assuming a molecular weight of 2.33.

The virial parameter α is estimated for each structure at each contour level, from the virial balance between the kinetic and gravitational potential energy, i.e. $\alpha = 2E_k/E_g$. Assuming a uniform density profile, this translates into:

$$\alpha = \frac{5\sigma_v^2 R}{M_{\rm CO} G} \quad \text{(A.2)}$$

where σ_v is the velocity dispersion and R is the size of the structure as estimated by the dendrogram code. Assuming a density profile as $\rho \propto r^{-2}$ would change the viral parameter by a factor of 3/5 (smaller). Without the presence of any additional terms in the virial equation (such as due to magnetic field or external pressure), the virial equilibrium corresponds to $\alpha = 1$. However, given the uncertainties associated with these assumptions, we consider a structure to be gravitationally bound when the virial parameter is less than 2. The use of such a parameter is best seen as an internal means of comparison of structures within the cloud than an absolute measure of the individual equilibrium states.

We performed this dendrogram analysis of B59 on the 3D datacubes of the intermediate density tracers ^{13}CO and C^{18}O. We considered the minimum height of a leaf to be one-sigma of the r.m.s. noise level, chose the bijection method to calculate the cloud properties (similarly to Rosolowsky et al. 2008).

A.2. Results

A.2.1. The ^{13}CO and C^{18}O dendrograms

The dendrograms for ^{13}CO and C^{18}O are shown in Fig. A.1, left and right panels respectively. This hierarchical stratification of ^{13}CO finds the entire structure of B59 to be interconnected and part of the same cloud, while with C^{18}O the cloud is no longer interconnected (likely due to signal to noise limitations). Despite the non-interconnectivity, the C^{18}O hierarchical stratification is consistent with that found with ^{13}CO though with less branching.

The properties of the dendrogram leaves are summarised on Tables A.1 and A.2. The first column indicates the region to which each leaf belongs to, and the second column shows the dendrogram ID number (cf. Fig. A.1, A.2 and A.3). The following columns show the properties derived at the lowest contour of each detected leaf: R is the radius; v_0 is the mean velocity, weighted by the intensity (with an uncertainty of 0.1 $\rm kms^{-1}$); σ_v is the velocity dispersion; M is the leaf mass (eq. A.1); and α is the virial parameter (eq. A.2). Bear in mind that the virial parameters shown in this table are estimated at the bottom of each leaf, but they evolve throughout the height of the leaves, generally approaching subvirial values (Fig. A.1). In addition, the row before-last shows the properties of the branch that covers the entire central region, and the last row shows the total mass, equivalent size and virial parameter of the entire B59. For ^{13}CO, the properties of the entire B59 were measured at the root of the dendrogram (root 44, Fig. A.1 left panel), while for C^{18}O this was estimated by combining the information of the three disconnected roots (Fig. A.1 right panel, roots 50, 47 and leaf 3).

These estimates do not account for the optical depth, which will particularly affect the central region of B59. A quantification of the possible optical depth effect for C^{18}O can be seen in the right panel of Fig. 4 as the deviations, at higher column

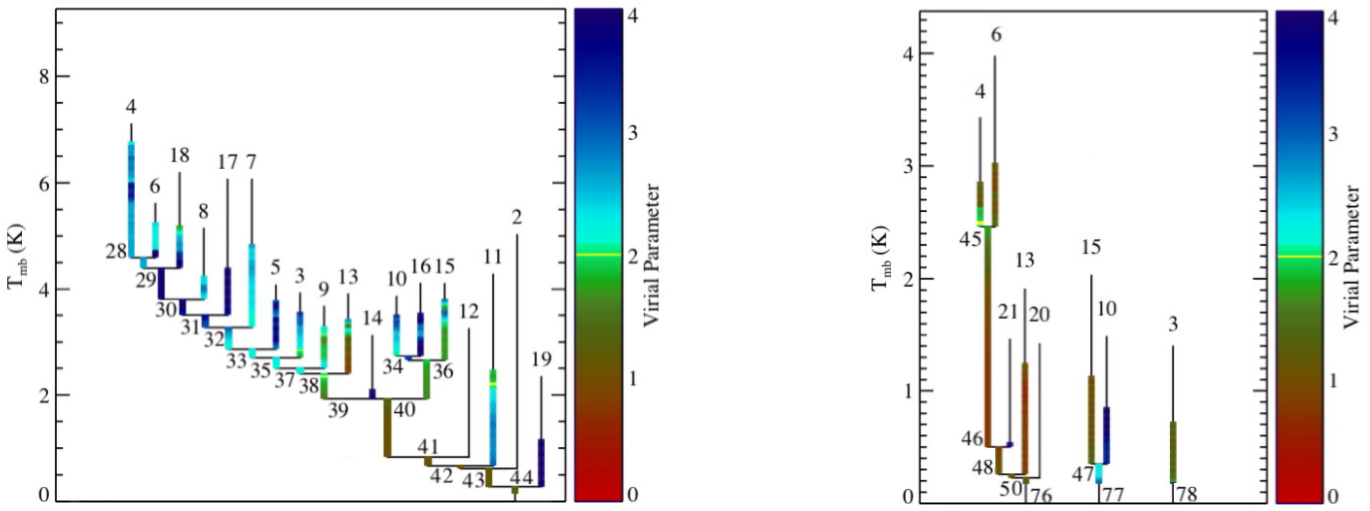

Fig. A.1. Dendrogram of the ^{13}CO (left) and C^{18}O emission (right) in B59, with the virial parameter calculated for each contour. The regions where no virial parameter is shown (e.g., the tips of the leaves) are due to the lack of sufficient quality data to calculate the properties, such as insufficient number of pixels.

Table A.1. Properties of the ^{13}CO dendrogram leaves

Region	Leaf #	R (pc)	v_0 (kms^{-1})	σ_v (kms^{-1})	M (M$_\odot$)	α
Central clump	4	0.03	3.9	0.19	0.63	2.3
	6	0.02	3.7	0.13	0.10	3.6
	18	0.02	2.9	0.13	0.10	3.7
	8	0.01	3.9	0.07	0.04	2.0
	17	0.04	3.2	0.15	0.31	3.2
	7	0.03	3.7	0.11	0.19	1.9
U-shaped ridge	5	0.06	3.9	0.14	0.57	2.5
	3	0.07	4.0	0.10	0.47	1.6
NE ridge	13	0.14	3.5	0.13	3.70	0.8
Western cores	10	0.05	3.4	0.14	0.63	1.9
	16	0.03	3.2	0.15	0.20	3.9
	15	0.06	3.4	0.15	1.15	1.5
SW lobe	9	0.04	3.6	0.11	0.28	1.9
SW lobe	14	0.03	3.4	0.08	0.06	3.6
NW lobe	11	0.04	3.5	0.11	0.21	2.6
NW lobe	19	0.04	2.2	0.20	0.13	13.6
Total Centre	(32)	0.11	-	0.33	7.87	1.9
Total	(44)	0.44	-	0.41	73.3	1.1

Table A.2. Properties of the C^{18}O dendrogram leaves

Region	Leaf #	R (pc)	V$_0$ (kms^{-1})	σ_v (kms^{-1})	Mass (M$_\odot$)	α
Central clump	4	0.02	3.4	0.14	0.19	1.6
	6	0.03	3.5	0.21	1.44	1.1
U-shaped ridge	3	0.06	3.4	0.13	0.91	1.5
NE ridge	13	0.15	3.5	0.15	5.82	0.7
Western cores	15	0.07	3.4	0.15	1.51	1.2
	10	0.07	3.3	0.21	1.15	2.9
West centre	21	0.05	3.5	0.17	0.52	3.3
Total Centre	(45)	0.10	-	0.29	16.1	0.7
Total		0.30	-	0.31	29.6	1.0

densities, above the green dashed line. This optical depth effect would account for a difference of $\sim$ 15% on average in the column density in this central region, which would translate into an equivalent increase of the mass estimate (and decrease of α).

A.2.2. The leaves of B59

The densest gas within the central clump of B59, is solely described by two leafs on both molecular lines, leaves 4 and 6, both gravitationally bound, and both at the systemic velocity of the cloud (in C^{18}O). These correspond to the two cores surrounding the youngest protostars of the region: B7, B8 and B11 within leaf 4, and B10 within leaf 6. Apart from these, we have four leaves with ^{13}CO in the central clump (leaves 7, 8, 17 and 18, labeled in red in Fig. A.2). These are a result of the ^{13}CO self absorption and outflow wings, which produce an overly sub-structured tree tracing outflowing gas at opposing velocities, and artificially separated by the self-absorption dip. These leaves do not have the systemic velocity of 3.5 kms^{-1} but they vary from 2.9 to 3.9 kms^{-1} and trace the dense outflowing gas from Flow 1.

The SE U-shaped ridge s divided in two halves with both isotopologues (labeled in yellow in Fig. A.2 and A.3). The lower-left half of the U-shaped ridge is identified with leaf 3, at slightly red-shifted velocities, consistent with the velocity map of C^{18}O (Fig. 9). The other half of the ridge is found as a red-shifted leaf in ^{13}CO (leaf 5), with a high virial parameter, consistent with compressed gas from the red outflow (Flow 2).

The entire NE ridge is found as leaf 13 (labeled in green in Fig. A.2 and A.3), without any sub-structure within, and at the systemic velocity of the cloud ($\sim$3.5 kms^{-1}). This is the only leaf in B59 that appears with a α below 1 with both ^{13}CO and C^{18}O.

On the other hand, the western cores branch out from the main tree and form a sub-structure on their own. They include leaves 10 and 15 (labeled in blue in Fig. A.2 and A.3), detected with both molecules. The mass and virial parameter of leaf 15, in particular, indicates that it could collapse to form future protostars, but at present it presents no evidence for ongoing star-formation. Despite a similar mass as the central cores of B59, its larger size (and therefore lower densities) are indicative of a less compact core which disposes of a smaller mass reservoir than the active star-forming cores. Spatially nearby, there is the blue-shifted ^{13}CO leaf 16, and the C^{18}O leaf 21, both with a high virial

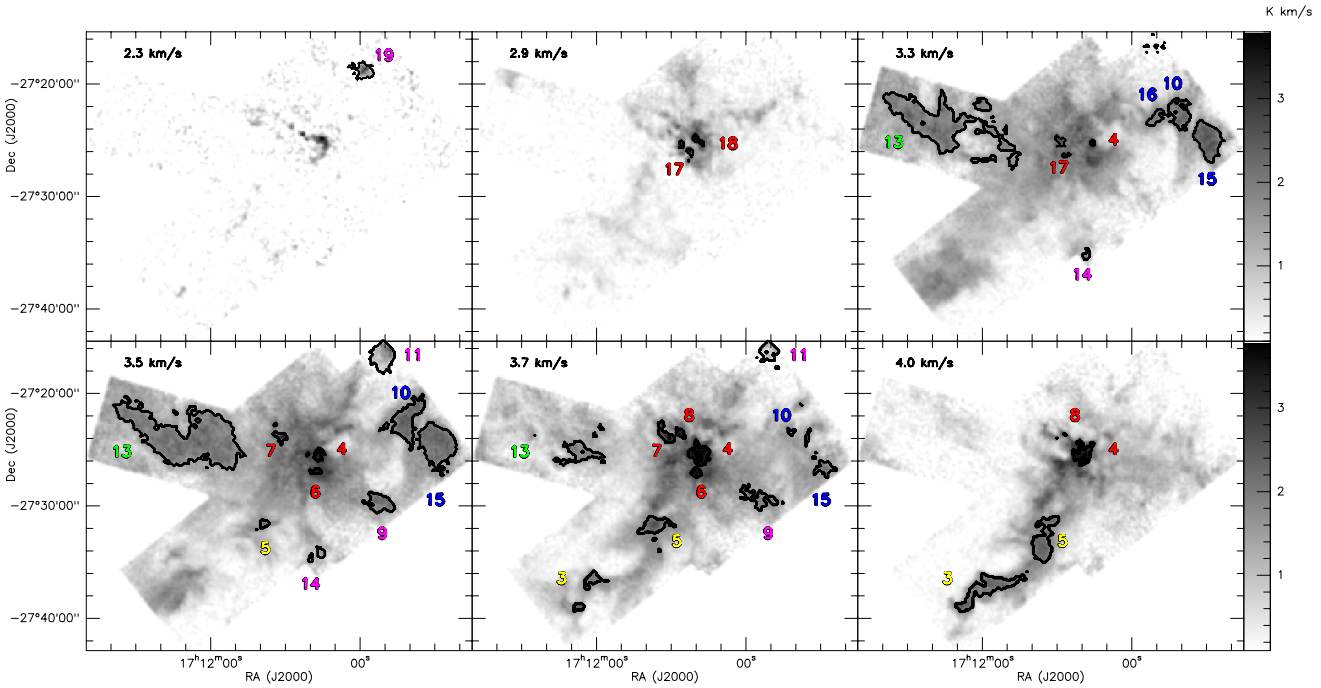

Fig. A.2. Six channel maps of the ^{13}CO emission T_A^*, whose velocities of are shown at the top-left corner of each panel. The plotted gray scale is that used for all panels with the exception of the first (top-left panel), where it is from 0.1 to 1.5 K kms^{-1}. The black contours show the positions of the leaves from Fig. A.1, whose numbering is colour-coded to visually separate the distinct areas: central region in red, NE ridge in green, SE U-shaped ridge in yellow, western cores in blue, and loose knots in purple.

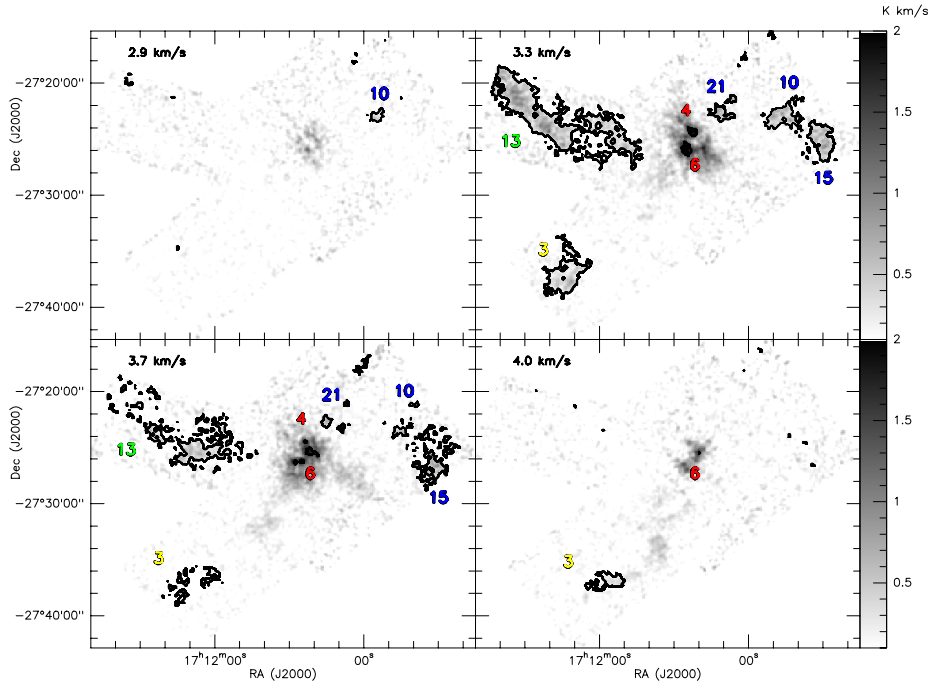

Fig. A.3. Four channel maps of the C^{18}O emission in T_A^* (in gray scale), whose velocities of are shown at the top-left corner of each panel. The black contours show the positions of the leaves from Fig. A.1, and are numbered accordingly. The colour code is the same as for Fig. A.2.

parameter. These two leaves lay at the edges of Cavity C, suggesting that they are part of the material pushed out of the cavity by an outflow. This gas-deprived cavity is now what physically separates the central region and the western cores.

Finally, we hypothesise that the ^{13}CO leaves 9, 11 and 14 (labeled in purple in Fig. A.2) are counterparts of the main outflows of the region, but since they do not present very large velocity offsets and since we cannot trace the material between these knots and the respective driving source, it is not trivial to understand their origin. Leaf 19, in particular, appears isolated and as a possible outflow bullet, with the highest virial parameter and the highest blue-shifted velocity in the cloud (at ~2.2 kms^{-1}).

A.2.3. The masses

A brief comparison of the masses derived from the ^{13}CO and C^{18}O emission shows that the structures which are common have similar mass estimates. C^{18}O recovers more mass from the NE ridge and some of the cores, as expected from the higher optical depth of ^{13}CO. Nevertheless, both lines show a total of ~ 10 M$_\odot$ comprised in the leaves. However, they differ in the total mass of the cluster by a factor of $\sim$2.5 (~ 74 M$_\odot$ with ^{13}CO versus ~ 32 M$_\odot$ with C^{18}O). Such a difference is mostly due to the diffuse gas mass present, traced only by ^{13}CO. That said, the fraction of mass comprised in the leaves is $\sim$11 % using the ^{13}CO, and $\sim$ 33% for the C^{18}O estimate.

Considering only the central clump of B59, our best mass estimate is retrieved from C^{18}O, as estimated at the lower level of branch 45. This central region is found to have a mass of ~ 16 M$_\odot$ within a region of ~ 0.1 pc radius, with an average velocity dispersion (σ_v) of 0.3 kms^{-1} (i.e. $\alpha = 0.7$).

When using the momuntum maps constructed over the entire velocity range, we retrieve, within a central region of $\sim$0.1 pc radii, a mass of 10 M$_\odot$, a mean velocity of 3.5 kms^{-1} and a mean σ_v of 0.35 kms^{-1}. Assuming the uniform profile as that taken for the dendrograms analysis, we retrieve a virial parameter of 1.5. The smaller mass estimated using the total integrated intensity is not surprising since we are now taking a circular area around the central region of 0.1 pc radii, out of which not all pixels are included in the calculation (due to a signal to noise limitation). For the same reason, the higher velocity dispersion is also compatible with the dendrograms, likely arising from the fact that the larger line widths in B59 are well concentrated in the central region. This is also clear if looking at the variations of the virial parameter of branch 45 (Fig. A.2, right), which start at $\sim$2 at higher levels, decreasing down to 0.7 at the lower level of the branch.